



Cite this: *Nanoscale Adv.*, 2021, **3**, 432

## Morphology dependent electrical conduction and breakdown in single $\text{TiO}_2$ nanotubes<sup>†</sup>

Sourav Kumar Kajli,<sup>a</sup> Debdutta Ray<sup>b</sup> and Somnath C. Roy  <sup>\*a</sup>

Understanding the electrical conduction properties of a single nanostructure is essential for gaining insight into the fundamental charge transport through 1D materials and also for exploring the collective behavior of an array of such nanostructures.  $\text{TiO}_2$  nanostructures, such as electrochemically grown nanotubes, have been widely studied in recent times for several applications. The electrolyte plays a vital role in deciding the morphology, which, in turn, governs the charge transport behavior. Here we present a comparative study of the charge transport through a single  $\text{TiO}_2$  nanotube grown by electrochemical anodization using ethylene glycol and dimethyl sulphoxide electrolytes. The individual nanotubes are assembled into nanodevices using photolithography without relying on complex and sophisticated process like electron beam lithography or focused ion beam deposition. The electric field dependent charge transport properties show Schottky emission at a lower field regime and Poole–Frenkel emission in the higher region. The temperature-dependent electrical conduction (110 K–410 K) is mediated by two thermal activation processes, attributed to shallow impurities in the low-temperature range ( $T < 230$  K) and to the donors at deep intermediate levels at higher temperatures ( $T > 230$  K). The activation energies for EG based nanotubes are found to be higher than those for DMSO nanotubes owing to the double wall morphology of the formed tubes. Also, the study of the electrical breakdown phenomena of these nanotubes reveals three distinct categories of collapse. 'Model A' type breakdown is characterized by a stepwise rise of the current up to the breakdown point and a fall to zero following a non-uniform step by step decrease, which is driven by crack formation near the electrode interface and its propagation. 'Model B' shows a transient rise and fall in current, leading to breakdown due to electromigration, whereas 'Model C' type breakdown observed in a bundle of nanotubes shows a mixed trend of 'Model A' and 'Model B'. The data and analysis provide insight into the current limit through an individual nanotube or bundle of nanotubes and will be useful for designing prototype nanodevices from titania nanostructures.

Received 25th August 2020  
Accepted 23rd November 2020

DOI: 10.1039/d0na00713g  
[rsc.li/nanoscale-advances](http://rsc.li/nanoscale-advances)

## Introduction

One-dimensional (1D) nanostructures such as nanowires,<sup>1</sup> nanotubes,<sup>2</sup> nanorods,<sup>3</sup> etc. show unique characteristics owing to a higher specific surface area and a directional charge flow. These properties make 1D nanostructures potential candidates for solar energy harvesting,<sup>2</sup> optoelectronic devices,<sup>4</sup> electrochemical energy conversion,<sup>5</sup> and chemical<sup>6</sup> and gas sensors.<sup>7</sup> Confinement in two dimensions allows movement of a majority of carriers along an axial flow configuration which also helps in separating electron–hole pairs as and when they are generated. Most of the reported work discussed arrays or bunches of nanostructures, wherein superior properties compared to those of polycrystalline materials or thin films were observed.

However, to realize the collective behavior of an array of nanostructures, investigation of the properties of a single nanostructure is necessary. It provides further depth to the applications once we understand the charge transport or current conduction through a single nanostructure. Also, it has the potential to solve the drawbacks and problems related to the efficiency or performance for a device application. It is reported that single nanostructures show promising behavior in sensing applications,<sup>8</sup> photovoltaics,<sup>9</sup> light emitting diodes,<sup>10</sup> transistors,<sup>11</sup> etc.

Titanium dioxide is one among the most extensively explored transition metal oxides having wide-scale applications such as in photocatalysis,<sup>12</sup> lithium-ion batteries,<sup>13</sup> gas sensing,<sup>14,15</sup> photoelectrochemical water splitting,<sup>16–18</sup> dye-sensitized solar cells,<sup>19–21</sup> disposable biosensors,<sup>22</sup> etc. In particular, titania nanotube arrays fabricated *via* electrochemical anodization have been widely studied in recent times, as is evident from the reviews.<sup>23–25</sup> Electrochemical anodization results in vertically aligned arrays of  $\text{TiO}_2$  nanotubes with varying geometrical features (length, diameter, and inter-tube

<sup>a</sup>Department of Physics, Indian Institute of Technology Madras, Chennai, Tamilnadu, 600036, India. E-mail: somnath@iitm.ac.in

<sup>b</sup>Department of Electrical Engineering, Indian Institute of Technology Madras, Chennai, Tamilnadu, 600036, India

† Electronic supplementary information (ESI) available. See DOI: [10.1039/d0na00713g](https://doi.org/10.1039/d0na00713g)



separation) and surface morphologies depending on the synthesis conditions. Although electrical devices are fabricated using two-point contact at the upper and lower end of the nanotube arrays, estimating charge transport in a single nanotube becomes difficult due to impurities or debris stuck on the pores or the inter-tubular spaces and inter-wall contacts. Literature reports suggest that a few studies have been performed to identify the electrical characteristics of single  $\text{TiO}_2$  nanotubes under various conditions. Fàbrega *et al.*<sup>26</sup> reported photoconduction in low resistivity  $\text{TiO}_2$  nanotubes fabricated using the DMSO electrolyte. They found that the charge carriers in these nanotubes recombine following the Hall–Shockley–Read mechanism of non-radiative recombination. Stiller *et al.*<sup>27</sup> studied electrical conduction in a single  $\text{TiO}_2$  nanotube and concluded that the electrical conduction is governed by the Mott variable range hopping mechanism. They also carried out impedance spectroscopy which revealed the dominance of grain cores in deciding the impedance characteristics. Hattori *et al.*<sup>28</sup> compared the electrical transport behavior of single anatase and rutile  $\text{TiO}_2$  nanotubes and showed that the charge conduction follows a metal–semiconductor–metal model with the presence of a Schottky junction. Lee *et al.*<sup>29</sup> carried out electrical conductivity studies on single  $\text{TiO}_2$  nanotubes using Pt interconnections made by e-beam and ion beam assisted deposition. They found that there exist about two orders of magnitude of difference in resistance depending on the deposition technique. Recently, Brahmi *et al.*<sup>30</sup> reported low-temperature n–p transition in single  $\text{TiO}_2$  nanotubes.

In the electrochemical anodization process, the morphology of the resultant nanotubes significantly depends on the electrolyte<sup>31,32</sup> used. For example, tubes with differences in wall thickness or smooth or granular surfaces and compact or separated nanotube arrays are formed with variations in the electrolyte. Such morphological differences are likely to affect the electrical properties of individual nanotubes, which, in turn, influence the performance of the fabricated devices. So far, a comparative study on the influence of morphology on the electrical conduction/charge transport in single  $\text{TiO}_2$  nanotubes has not been carried out. In this work, we present temperature-dependent electrical conduction studies on single  $\text{TiO}_2$  nanotubes obtained by electrochemical anodization in  $\text{NH}_4\text{F}$ /ethylene glycol (EGTNT) and dimethyl sulfoxide (DMSO)/HF (DMTNT) electrolytes. The use of EG and DMSO based electrolytes results in markedly different morphologies; for example, smooth and double-walled nanotubes (DWNT) in EG and rough, single-walled nanotubes (SWNT) in DMSO. Further, the aim of the study is to understand how a single  $\text{TiO}_2$  nanotube behaves under an applied bias and to what extent it is capable of withstanding the current flow. Although a majority of studies have been reported on the applications of  $\text{TiO}_2$  nanotube arrays (bundles), there are also a few reports on the use of single nanotubes for applications such as biosensors,<sup>33</sup> gas sensors,<sup>34</sup> etc. The gas or any particular adsorbate to be sensed is adsorbed at the surface of the sensing materials. The semiconducting nature of the  $\text{TiO}_2$  nanotube ensures heating of the surface under the application of a voltage through Joule heating. Because of the higher surface to volume ratio, even a small

current can result in significant heating in the nanostructure, which, in turn, can tune the adsorption of the adsorbates in a favorable way. The single nanostructure such as the  $\text{TiO}_2$  nanotube can therefore act as a low power consuming, self-heating sensor under a nominal bias. However, to further explore such applications, a thorough understanding of the charge transport and its dependence on morphology is essential.

So, we have analyzed the limit of compliance and onset of catastrophic failure (breaking of nanotubes due to Joule heating) in these individual  $\text{TiO}_2$  nanotubes. The results provide a thorough insight into the electrical behavior and breakdown and also establish a platform for future device applications involving single  $\text{TiO}_2$  nanotube devices.

## Experimental

### Materials and device fabrication

Electrochemical anodization was performed in a two-electrode cell consisting of a Ti foil anode and a Pt cathode. Anodization was implemented using two different electrolyte media, ethylene glycol (EG) and dimethyl sulfoxide (DMSO), to obtain nanotubes with two distinct morphologies. The EG based electrolyte comprises 0.25 wt%  $\text{NH}_4\text{F}$ , 2 ml DI water, and 98 ml ethylene glycol, while for DMSO, the electrolyte comprises 2 vol% HF and 98 vol% DMSO. The anodization was accomplished under potentiostatic conditions by applying 60 V for 4 hours and 50 V for 12 hours, respectively, for EG and DMSO based electrolytes. Afterward, the Ti foil samples containing vertically grown  $\text{TiO}_2$  nanotubes were dried and annealed in a furnace at 450 °C in air for 2 hours. The crystallinity of EGTNT and DMTNT was characterized using a Rigaku smartlab X-ray diffractometer (Fig. S1 in the ESI†), and the surface morphologies of the nanotube (NT) arrays were observed using an FEI Inspect F50 scanning electron microscope (SEM). The SEM images in Fig. 1(a) and (b) show that the average pore diameters are about 104 nm and 149 nm for EGTNT and DMTNT, respectively. The diameters and wall thickness of the nanotubes were measured from the FESEM images using ImageJ software. Electrical contacts to individual nanotubes were fabricated by using photolithography, metallization, and the lift-off process. Prior to this, the anatase titania NTs were removed from the titanium substrate by ultrasonication in ethanol, and a resultant dispersion was obtained. A p-type Si wafer of size 3.5 cm × 3.5 cm was used on which a 70 nm  $\text{SiO}_2$  layer was grown as an insulator. The electrodes (5 nm Cr/35 nm Au) of sizes 100  $\mu\text{m}$  × 100  $\mu\text{m}$  were fabricated on the Si/ $\text{SiO}_2$  substrate by photolithography, electron beam evaporation, and the lift-off process to obtain the final patterned substrate. The  $\text{TiO}_2$  nanotubes were transferred by drop-casting 10  $\mu\text{l}$  of the dispersion ( $\text{TiO}_2$  NTs in ethanol) onto the patterned Si substrate. After depositing the NTs onto the array of electrodes, a high-resolution scanning electron microscope was used to locate single NTs that formed bridges between two electrodes, and the exact location was listed with the column and row numbers of the electrodes. This process is a simple, relatively inexpensive, and faster process for the fabrication of single nanotube devices compared to other sophisticated techniques like e-beam lithography and focused



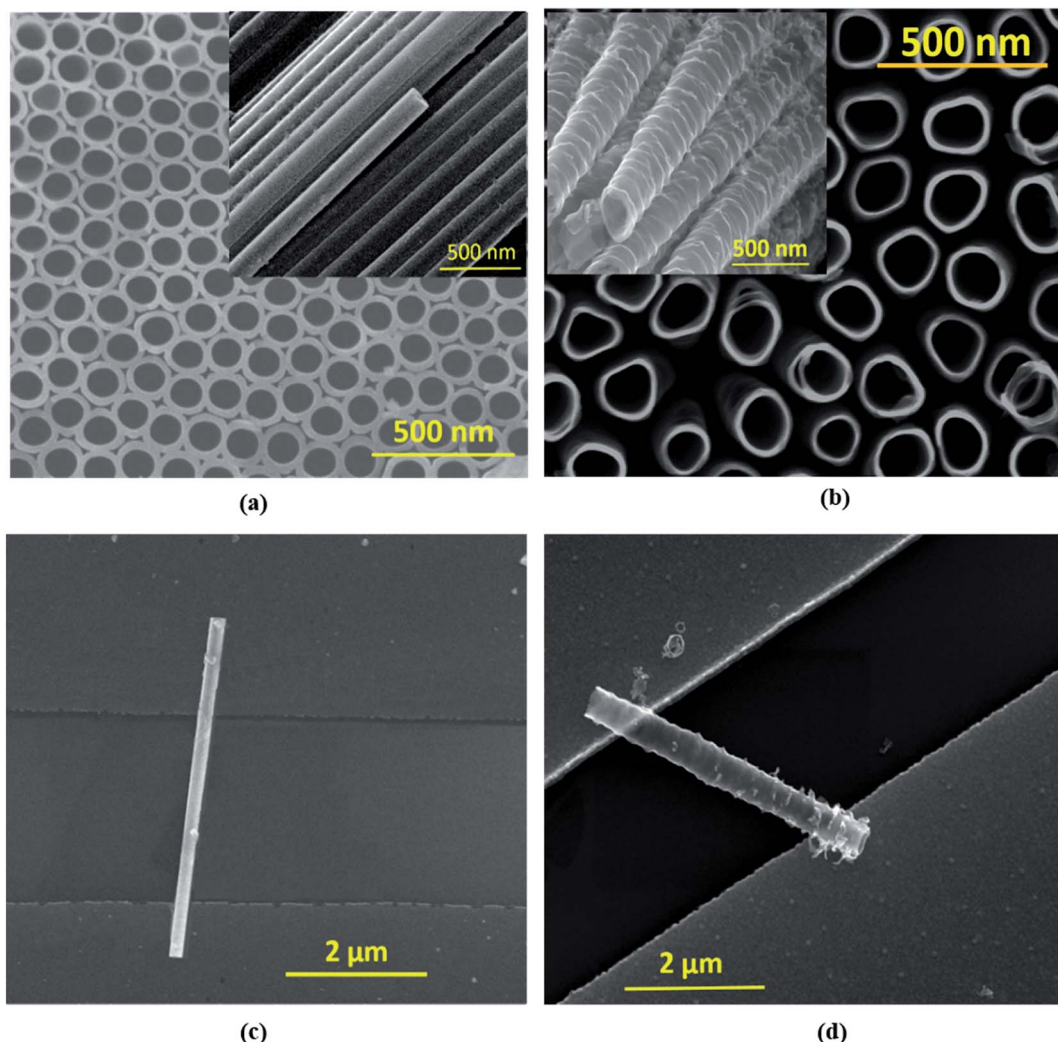


Fig. 1 FESEM image showing the top and side view (inset) of (a) EGTNT and (b) DMTNT and (c) and (d) show the individual  $\text{TiO}_2$  nanotube devices of EGTNT and DMTNT, respectively, on Au electrodes on top of the  $\text{SiO}_2/\text{Si}$  substrate.

ion beam. The Si wafer containing  $\text{TiO}_2$  nanotubes was annealed at 150 °C for 30 min under  $\text{N}_2$  to ensure good contact between nanotubes and electrodes and to eliminate any unwanted absorbed moisture or volatile contaminants.<sup>35,36</sup> The individual nanotubes of EGTNT and DMTNT on Cr/Au electrode pads are displayed in Fig. 1(c) and (d). The electrical characterization of the individual nanotubes was performed by analysis of temperature-dependent  $J$ - $V$  characteristics measured in a vacuum chamber ( $10^{-5}$  mbar) with two probe measurements using a Semiconductor Device Parameter Analyzer (Keysight B1500A). The data analysis and curve fitting were carried out using Origin 8.5 software.

## Results and discussion

### Temperature-dependent and field-dependent electrical characteristics

The current density-applied bias ( $J$ - $V$ ) plots for individual EGTNT and DMTNT at room temperature are presented in

Fig. 2(a). Since the conductivity of materials is governed by the carrier concentrations and mobility of the charge carriers, temperature-dependent  $J$ - $V$  characteristics were obtained in the range of 110 K–410 K at an interval of 20 K. The data for EGTNT and DMTNT are presented in Fig. 2(b) and (c), respectively. The study shows that the current increases with temperature for both forward and reverse biases implying a typical semiconducting behavior.

Now, the nanotube can be considered to be a hollow cylinder, and the effective cross-sectional area can be obtained using  $A = \frac{\pi}{4} (D_2^2 - D_1^2)$  where  $D_2$  and  $D_1$  are the external and internal diameters of the nanotube, respectively. For EGTNT, the average  $D_2$  and  $D_1$  values are 151 nm and 104 nm, and for DMTNT, the average magnitudes of  $D_2$  and  $D_1$  are 188 nm and 149 nm, respectively (Fig. 1(a) and (b)), measured using ImageJ software. The approximate conductivity value ( $\sigma$ ) can be obtained using  $\sigma = \frac{I}{V} \times \frac{L}{A}$ , where  $A$  and  $L$  represent the cross-sectional area and length of the nanotube, respectively. The



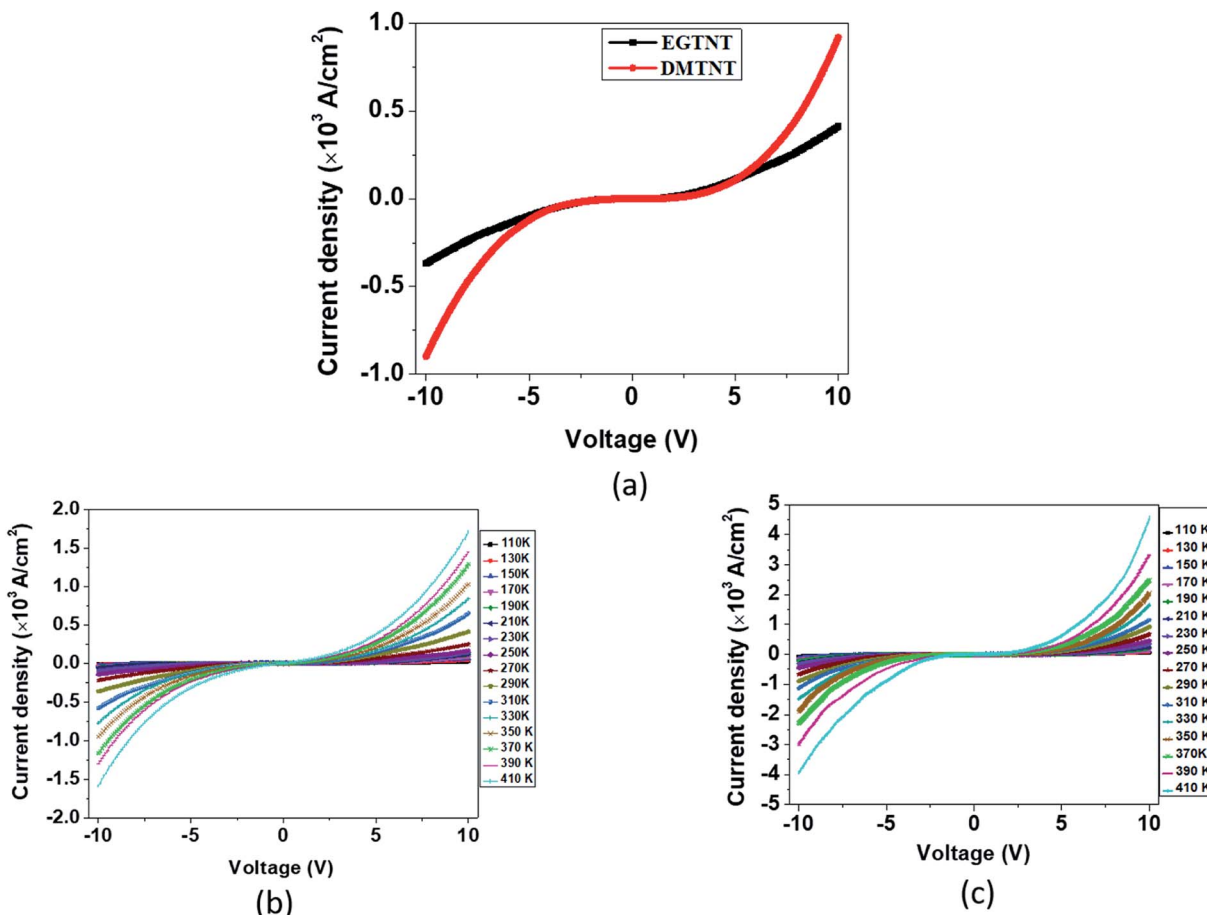


Fig. 2 Current density–voltage ( $J$ – $V$ ) plots (a) for EGTNT and DMTNT at room temperature, (b) for the individual EGTNT at different temperatures and (c) for the individual DMTNT at different temperatures.

SEM images in Fig. 1(c) and (d) show estimated effective lengths ( $L$ ) of the  $\text{TiO}_2$  nanotube of about 2.61  $\mu\text{m}$  and 3.02  $\mu\text{m}$  for EGTNT and DMTNT, respectively, measured using ImageJ software. Therefore, the conductivity of the  $\text{TiO}_2$  nanotube, derived by assuming zero contact resistance, is given by  $\sigma \approx 1.08 \times 10^{-2}$  S cm $^{-1}$  for EGTNT and  $2.77 \times 10^{-2}$  S cm $^{-1}$  for DMTNT, respectively. These values are close to the reported conductivity of polycrystalline  $\text{TiO}_2$  nanotubes.<sup>37</sup>

The electrical transport in a semiconducting material can be classified into two categories: electrode limited conduction and bulk limited conduction. The electrode limited conduction mechanisms comprise Schottky or thermionic emission, Fowler–Nordheim tunneling, *etc.* On the other hand, the bulk limited mechanisms are Poole–Frenkel emission, hopping, space charge limited current, *etc.* Each of these has characteristic  $J$ – $V$  plots with the precise nature of temperature dependence. Therefore, a thorough analysis of the  $J$ – $V$  data at different temperatures reveals the appropriate behavior of the charge transport mechanism.

The Schottky mechanism, which is electrode limited conduction, is governed by the potential barrier ( $\phi_{\text{sc}}$ ) at the electrode–semiconductor interface and influenced by both

temperature ( $T$ ) and electric field ( $E$ ). The current density ( $J_{\text{sc}}$ ) under the Schottky mechanism<sup>38,39</sup> is given as

$$\ln J_{\text{sc}} = \frac{\beta_{\text{sc}}}{kT} \sqrt{E} + \left[ \ln AT^2 - \frac{q\phi_{\text{sc}}}{kT} \right] \quad (1)$$

where  $\beta_{\text{sc}}$  is expressed as  $\beta_{\text{sc}} = \sqrt{\frac{q^3}{4\pi\epsilon_0\epsilon_r}}$ ,  $k$  is the Boltzmann constant,  $A = \frac{4\pi q m^*}{h^3}$ ,  $q$  is the electronic charge,  $\epsilon_0$  is the permittivity of free space,  $\epsilon_r$  is the dynamic dielectric constant of the material,  $m^*$  is the effective mass of electrons and  $h$  is the Planck constant. Eqn (1) helps us to calculate the barrier height at the electrode–semiconductor interface if the temperature-dependent current–voltage characteristics are known. In addition, the dynamic dielectric constant of the semiconductor can also be derived from the slope of the  $\ln J_{\text{sc}}$  vs.  $E^{1/2}$  plot.

On the other hand, the bulk limited Poole–Frenkel (P–F) mechanism is governed by the movement of charge carriers from traps to the conduction band of the semiconductor by applying an electric field. A reduction in the Coulomb potential energy stimulates the release of charges from trap states, and the amount of reduction in potential energy is proportional to the probability of a charge carrier being thermally excited out of

the traps. The equation relating current density  $J_{\text{PF}}$  under P-F emission is given by

$$J_{\text{PF}} = CE \exp \left[ -\frac{q(\phi_t - \sqrt{qE/\pi\epsilon_0\epsilon_r})}{kT} \right] \quad (2)$$

where  $C = q\mu N_c$ ,  $\mu$  is the mobility of electrons,  $N_c$  is the density of states in the conduction band,  $E$  is the electric field,  $\phi_t$  is the barrier height for the emission of electrons from trap states,  $q$  is the charge of an electron,  $k$  is the Boltzmann constant,  $T$  is the temperature, and  $\epsilon_0$  and  $\epsilon_r$  are the permittivity of free space and the dynamic dielectric constant of the material, respectively.

Eqn (2), in particular, helps us to calculate the barrier height for the emission of charge carriers from trap states into the conduction band and also the dynamic dielectric constant of the semiconducting material from the slope of the  $\ln(J/E)$  vs.  $E^{1/2}$  plot. To obtain a proper realization of the dominant transport mechanism,<sup>38</sup> the current density  $J$  and  $J/E$  are plotted as a function of the square root of the electric field  $E$  in the semi-logarithmic plot, as shown in Fig. 3. The Schottky mechanism is dominant at a lower electric field, whereas the P-F mechanism is dominant at a higher field. Because of the difference in functional dependence between  $J$  and  $E$  for these two

mechanisms, the slopes of the plots are characteristically different when these two mechanisms operate in different ranges of the electric field. A careful look at the data reveals that slopes of the respective curves have a “change over” at about  $13\ 000\ \text{V cm}^{-1}$  for EGTNT (Fig. 3(a)) and about  $16\ 600\ \text{V cm}^{-1}$  for DMTNT (Fig. 3(c)). The lower slope regions below these values are analyzed according to Schottky emission, whereas the higher slope regions greater than these values are analyzed as the P-F mechanism.

Analysis of the data indicates that the electrical transport can be explained by a linearly fitted curve (using Origin 8.5 software) in the lower regimes of the electric field, up to approximately  $13\ 000\ \text{V cm}^{-1}$  and  $16\ 600\ \text{V cm}^{-1}$  for EGTNT and DMTNT, respectively, indicating the Schottky emission (illustrated in Fig. 3(a) and (c)). As the electric field increases beyond these values (approximately  $15\ 000\ \text{V cm}^{-1}$  and  $17\ 000\ \text{V cm}^{-1}$  for EGTNT and DMTNT, respectively), the Poole–Frenkel (P-F) mechanism dominates,<sup>40</sup> as displayed in Fig. 3(b) and (d). Poole–Frenkel emission implies a mechanism that occurs at a high field and is similar to the Schottky emission, where charge carriers move from a trap state to the conduction band (CB) *via* thermal excitation and the electric field. The dielectric

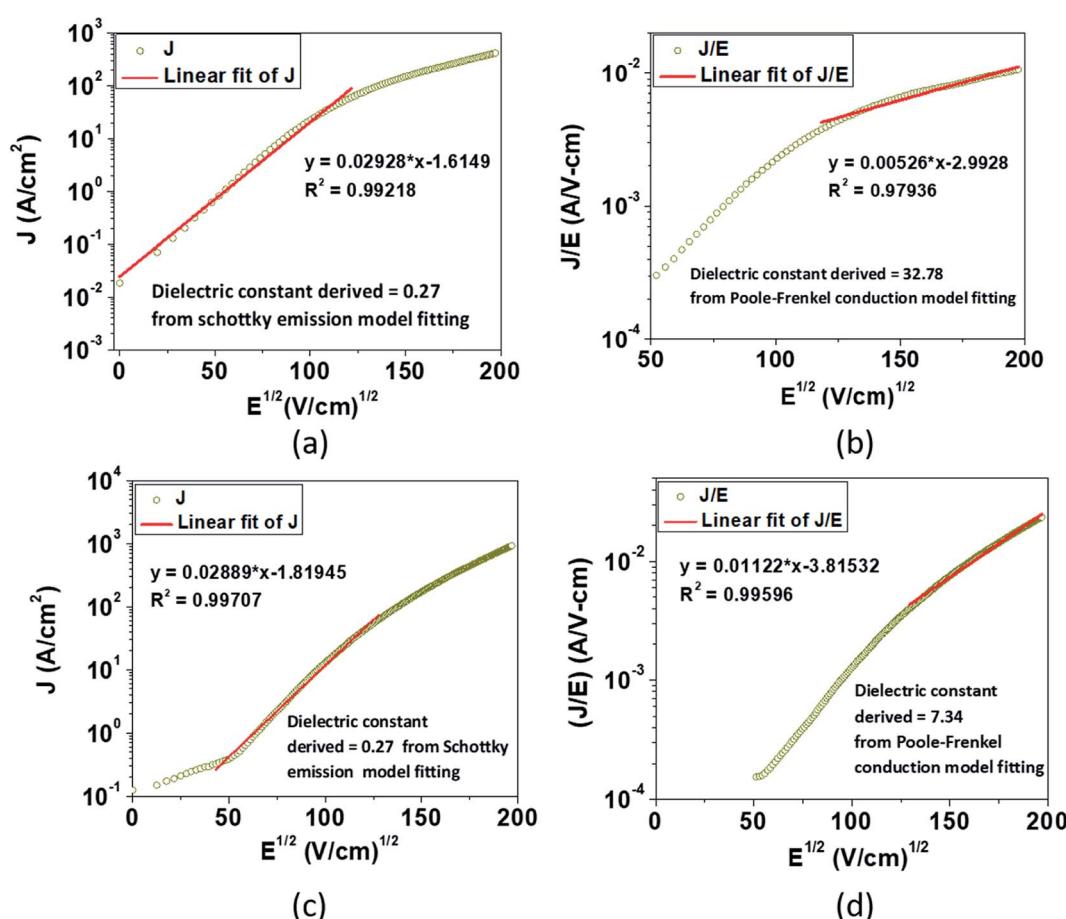


Fig. 3 The experimental semi-logarithm plot of  $J$  vs.  $E^{1/2}$  according to eqn (1) for (a) EGTNT and (c) DMTNT at 290 K in the lower bias region; the experimental semi-logarithm plot of  $(J/E)$  vs.  $E^{1/2}$  according to eqn (2) for (b) EGTNT and (d) DMTNT at 290 K in the higher electric field area. The red straight line denotes the fitting curve to those specified equations in a fixed range of the electric field.



constant values obtained from the slope of the curves fitted to eqn (1) and (2) are tabulated in Table 1 and are the values at higher frequencies,<sup>41</sup> not the static dielectric constant, as the electrons released from the trap state cannot polarize the surrounding medium. The magnitudes of  $\epsilon_r$  are in good accord with the earlier published values of titania thin films<sup>42</sup> and nanotubes.<sup>43,44</sup>

The dielectric constant values are derived from slopes  $\frac{\beta_{sc}}{kT}$  and  $\frac{\beta_{PF}}{kT}$  of the respective  $J$ - $E$  plots (Fig. 3). Now keeping the temperature constant (*i.e.*,  $kT$  is constant), in the case of the

Schottky mechanism, the slope  $\beta_{sc}$  is given by  $\beta_{sc} = \sqrt{\frac{q^3}{4\pi\epsilon_0\epsilon_r}}$  whereas for the Poole–Frenkel (P–F) mechanism, the slope  $\beta_{PF}$  is given by  $\beta_{PF} = \sqrt{\frac{q^3}{\pi\epsilon_0\epsilon_r}}$ .

Here, in both cases, the dielectric constant ( $\epsilon_r$ ) is inversely proportional to the square of the slope. Now, as observed in Fig. 3, the slope of the curve in the Schottky region is higher than that in the P–F region, which gives lower values of the dielectric constant derived from the Schottky mechanism compared to that from the P–F mechanism. A similar trend was also observed by Yang *et al.*<sup>42</sup>

The data reveal that the dielectric constant values derived from the Schottky mechanism are 0.27 for both EGTNT and DMTNT. It should be noted that the values derived from the

Schottky mechanism are unrealistically low. On the other hand, the dielectric constant values derived from the P–F mechanism are 32.78 and 7.34 for EGTNT and DMTNT, respectively. The double-walled morphology of EGTNT results in additional polarization effects, and hence the dielectric constant increases. Such values are also reported by terahertz spectroscopy for EG based  $\text{TiO}_2$  nanotubes.<sup>43,44</sup>

The current density is dependent on both the concentration and mobility of the charge carriers, both of which are functions of temperature. When the current densities are plotted as a function of  $1/T$ , the slope of the curve gives information about the activation energy, which is an important parameter for charge conduction. The current density is plotted with respect to  $1/T$  at different voltages to ascertain if the activation energy has voltage dependence. The experimental plots of the measured current densities at different voltages (5 V, 7 V, and 10 V) with the inverse of temperature are shown in Fig. 4. The plots have two linear segments with distinct slopes corresponding to various temperature ranges of  $\sim 110$ – $230$  K (small dotted line) and  $\sim 230$ – $410$  K (straight line), respectively. An Arrhenius type response signifies that the charge conduction occurs due to the thermal activation processes. Based on the obtained data, the total measured current density  $J$  for the entire temperature range can be expressed as

$$J = J_1 \exp\left(\frac{-E_1}{kT}\right) + J_2 \exp\left(\frac{-E_2}{kT}\right) \quad (3)$$

where  $k$  is the Boltzmann constant,  $T$  is the temperature,  $J_1$  and  $J_2$  are temperature independent pre-factors, and  $E_1$  and  $E_2$  are the related activation energies corresponding with the two kinds of thermal activation mechanisms.

The values of activation energies derived from the slope of the  $\ln J$  vs.  $1/T$  plot at 10 V are  $E_1 \sim 122 \pm 5$  meV and  $E_2 \sim 33 \pm 1$  meV for EGTNT and  $E_1 \sim 115 \pm 4$  meV and  $E_2 \sim 28 \pm 2$  meV for DMTNT. It should be mentioned that these values are almost similar for other bias voltages, *i.e.*, 5 V and 7 V. These

Table 1 Values of the dielectric constant derived from charge transport mechanisms

Types of $\text{TiO}_2$ nanotube	Schottky mechanism	Poole–Frenkel mechanism
EGTNT	0.27	32.78
DMTNT	0.27	7.34

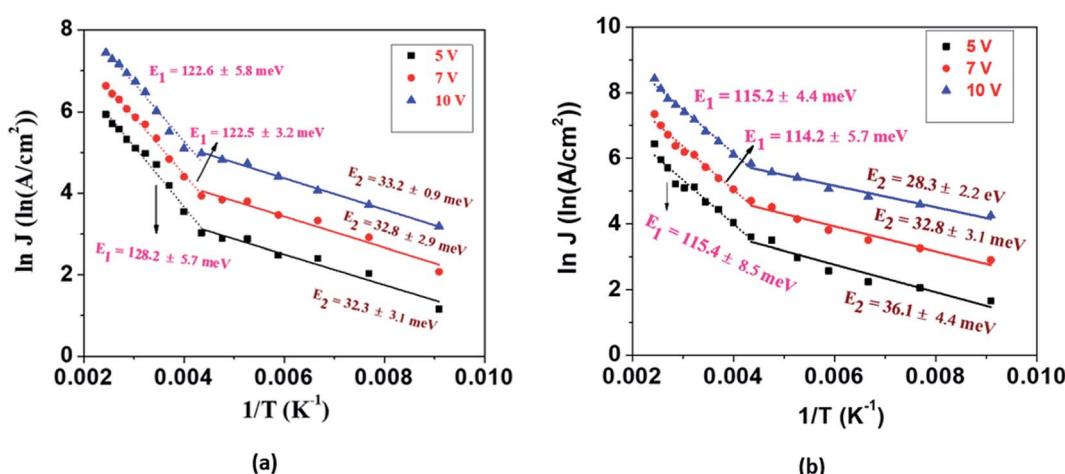


Fig. 4 Logarithm of current density ( $J$ ) as a function of the reciprocal of the temperature between 110 K and 410 K at 3 different bias voltages (a) for individual EGTNT and (b) for individual DMTNT showing intermediate deep and shallow donor levels  $E_1$  and  $E_2$ , respectively. The symbols are the experimental data and the straight lines and dotted lines are the linearly fitted curves to the data.



observations indicate that there exist two trap levels consisting of deep intermediate donors and shallow donors associated with the activation energy of  $E_1$  and  $E_2$ , respectively. At  $T > 290$  K (*i.e.*,  $1/T < 0.0034$  K $^{-1}$ ), both types of donor levels are activated by injecting charges into the conduction band that take part in the electrical conduction. As the temperature decreases below 230 K (*i.e.*,  $1/T > 0.0043$  K $^{-1}$ ), the donors at deep intermediary levels are no longer available even though the shallow donors contribute to the charge transport.

It should be mentioned that the obtained values of  $E_1$  and  $E_2$  for both EGTNT and DMTNT are in decent agreement with the localized trap state of 133 meV below the CB state and activation energy of 28 meV as reported previously by Mohammadpour *et al.*<sup>45</sup> and Chen *et al.*<sup>46</sup> respectively. The magnitudes of the activation energy correspond to shallow impurities, for example, oxygen vacancies, which are introduced during the growth or annealing process of the TiO<sub>2</sub> nanotubes. A substantial quantity of oxygen vacancies gives rise to a significant distribution of the donor or ionization energy levels, and consequently, the impurity band gets created. Previously, an activation energy of 58 meV for TiO<sub>2</sub> nanowires was obtained by Baik *et al.*<sup>47</sup> and Rothschild *et al.*<sup>48</sup> reported activation energy values of 0.01–0.69 eV with the variation of the ambient air pressure for nanocrystalline TiO<sub>2</sub> films. So, it should be pointed out that TiO<sub>2</sub> nanostructures grown by diverse methods (synthesized by different processes) and under different conditions can have dissimilar donor concentrations resulting in various values of the activation energy. Despite having a similar crystal structure (XRD patterns showing the anatase phase of both EGTNT and DMTNT are presented in Fig. S1 in the ESI†), the charge flow along the EGTNT encounters inter wall boundaries because of the double-wall morphology, while the charges flowing through the DMTNT see a relatively smoother conduction pathway, leading to lower activation energy values compared to their EGTNT counterparts. Although the morphological difference in EGTNT and DMTNT has been reported in the literature, our data present the first detailed analysis of the temperature-dependent transport and activation energy determination for the observed morphological variation.

In a semiconducting material such as TiO<sub>2</sub>, donor density  $N_d$  plays a direct role in determining the current–voltage characteristics which in turn control the device behavior. The donor density is therefore of primary significance for the determination of electrical properties. A direct experimental determination is challenging due to the involvement of a number of factors. For example, Mott–Schottky measurements provide information about  $N_d$ , but the actual interfacial surface area of the semiconductor contact with the electrolyte is very difficult to determine accurately. However, we can approximate the shallow

and intermediate donor concentrations from the extracted  $J_2$  value (associated with  $E_2$ ) and  $J_1$  value (associated with  $E_1$ ) in eqn (3). We can estimate the pre-factors  $J_1$  and  $J_2$  from the intercept of the  $\ln J$  vs.  $1/T$  plot, which can be related with the donor density  $N_d$  as

$$J = N_d q \mu E \quad (4)$$

where  $J$  is the current density,  $N_d$  is the donor concentration,  $e$  is the electronic charge,  $\mu$  is the electron mobility, and  $E$  is the applied electric field. The calculated values of  $N_{d1}$  and  $N_{d2}$  are presented in Table 2, where  $N_{d1}$  is the intermediate donor concentration and  $N_{d2}$  is the shallow donor concentration. Although the values are of the same order of magnitude for both types of nanotubes ( $\mu = 3.6$  cm $^2$  V $^{-1}$  s $^{-1}$ )<sup>28</sup> there is a difference in donor density in the two types of NTs. Due to the higher donor density a broader defect band is formed in DMTNT. This also contributes to a lower value of activation energy<sup>49</sup> in comparison with that of EGTNT.

The strikingly different morphologies of TiO<sub>2</sub> NTs synthesized *via* anodization depending on the electrolytes used were reported by Liu *et al.*<sup>50</sup> The ‘single-walled’ NT is DMSO based and ‘double-walled’ NT grows in the EG electrolyte. The EG based electrolyte is widely used<sup>23</sup> in TNT synthesis and results in double-walled structures with prolonged growth and partial crystallization of the tubes during the growth process. The schematic representation of single-walled and double-walled morphology for DMTNT and EGTNT is displayed in Fig. 5(a) and (b), respectively. SEM images of the bottom part and top part are shown in Fig. 5 showing the variation of the inner diameter from the upper to the lower part of the nanotube arrays to demonstrate the difference in wall morphology.

During anodization at a voltage of 60 V, substances decomposed from EG and fluoride ions feasibly undergo reaction with Ti<sup>4+</sup> ions at the EG–TiO<sub>2</sub> boundary and develop the interior wall<sup>50</sup> of the DWNT, consequently increasing the carbon impurities. The double-walled feature of the tubes becomes noticeable in the SEM images after annealing. To avoid the development of the contaminated inner wall, we should use the type of electrolyte (*i.e.*, DMSO mixed with HF) that leads to a greater extent of Ti<sup>4+</sup> dissolution and also limits the formation of undissolved residues. As suggested by Mirabolghasemi *et al.*,<sup>51</sup> a DMSO based electrolyte has the capability to dissolve by-products formed during anodization.

When the nanotubes are formed in DMSO electrolytes, they have a larger inner diameter with persistent wall thickness all the way through the whole length (Fig. 5(c)). The residual debris like carbon or fluorine species gets trapped in the inner shell and gets dissolved in the form of [TiF<sub>6</sub>]<sup>2-</sup>. The inner wall becomes thinner towards the tube top, indicating complete

Table 2 Estimated values of the shallow and intermediate deep donor concentration in EGTNT and DMTNT

Type of nanotube	Value of $E_1$ (meV)	Value of $E_2$ (meV)	Value of $N_{d1}$ (cm $^{-3}$ )	Value of $N_{d2}$ (cm $^{-3}$ )
EGTNT	132.1	32.9	$2.56 \times 10^{18}$	$3.65 \times 10^{16}$
DMTNT	115.2	28.3	$4.44 \times 10^{18}$	$5.59 \times 10^{16}$



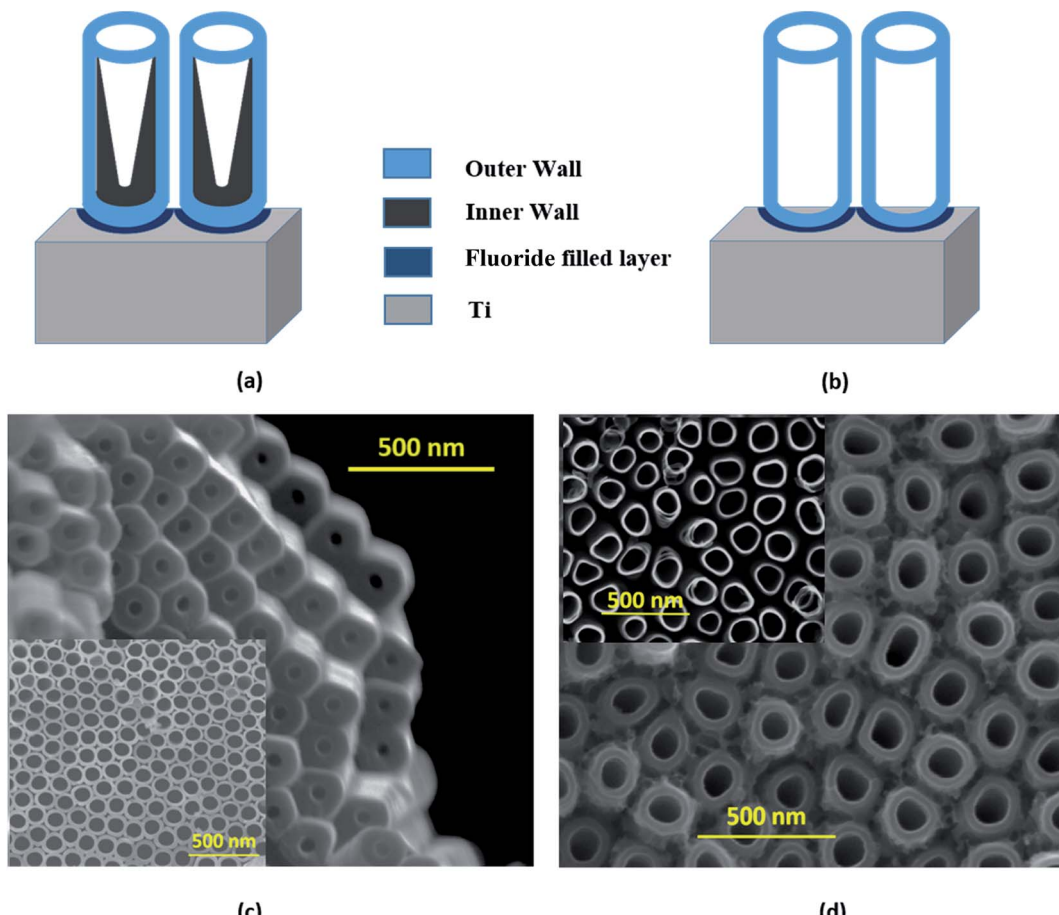


Fig. 5 Schematic representation of the double walled and single walled morphology for (a) EGTNT and (b) DMTNT, respectively. SEM images of the bottom part and top part (inset) of (c) EGTNT and (d) DMTNT showing the variation of the pore diameter from the top part to the bottom part for the nanotube arrays.

decomposition of the debris near the tube opening. Post the annealing process, the single-walled tubes show considerably different physical properties than their double-walled counterparts. It was reported by Mirabolghasemi *et al.*<sup>51</sup> that the annealed SWNT reveal a substantial enhancement of their electrical conductivity compared to DWNT, which has also been reflected in our experiments, where the conductivity of individual SWNT is much higher than its DWNT counterpart. The variation of activation energies ( $E_1$  and  $E_2$ , as shown in Table 2) in EGTNT and DMTNT can be understood by considering this morphological variation of the walls of the nanotubes.

#### Catastrophic breakdown in the $\text{TiO}_2$ nanotube

During the  $I$ - $V$  measurements on single nanotubes, we observed physical breakdown (breaking or collapse) under certain conditions, which are presented in Fig. 6–8. In order to understand the capability and limitations of charge transport through these nanostructures, we need to analyze such breakdowns in greater detail.

Tian *et al.* recently reported HR-TEM studies of the breakdown in  $\text{TiO}_2$  nanocrystals.<sup>52</sup> *In situ* microscopy was performed to understand the physical characteristics associated with such

breakdowns in  $\text{TiO}_2$  nanocrystals. In the case of  $\text{TiO}_2$  nanotubes, however, we have observed three types of  $J$ - $V$  plots during the breakdown, which are described as 'Model A' (Fig. 6), 'Model B' (Fig. 7) representing single DMTNT, and 'Model C' (Fig. 8) representing a bundle of EGTNT. In general (common to all figures), at lower applied potential (less than 1 V), the current density  $J$  is almost linear and subsequently becomes nonlinear with an increase in voltage which finally culminates in breakdown through three different approaches.

In the first approach (Model 'A', Fig. 6), a small transient increase of  $J$  up to  $-6.2$  V followed by a stepwise rise up to the breakdown point ( $-10$  V) and then a fall to zero with a non-uniform step by step decrease ( $-10$  V to  $-16.6$  V) is observed. The SEM images of a single NT before and after the breakdown are shown in Fig. 6(b) and (c). The stepwise reduction of  $J$  may signify crack formation and its progress in the wall of  $\text{TiO}_2$  NTs, leading to collapse, which we label 'Model A' breakdown. The noisy nature of the current density profile is directly related to the creation of "breakdown paths" or cracks, which possibly induce trapping and de-trapping of charge carriers. The charges, unable to obtain an easy pathway, start accumulating, leading to a local 'hot zone' that creates further cracks. The

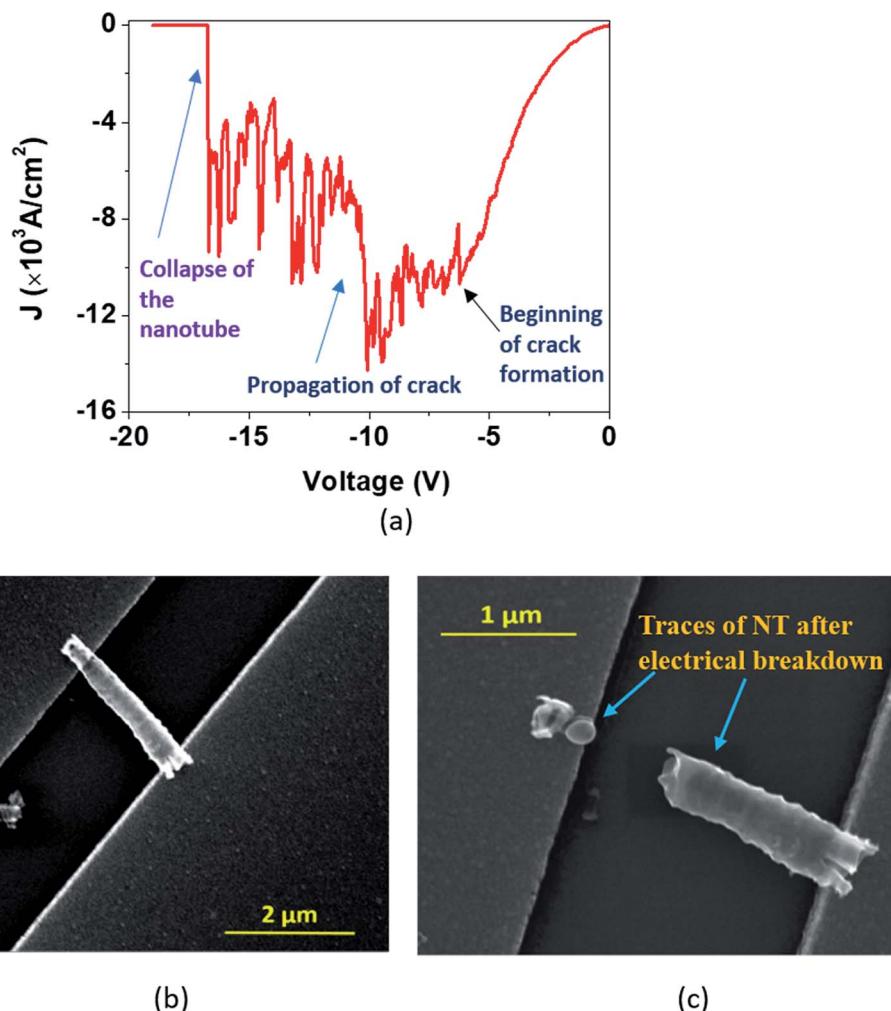


Fig. 6 (a) In the 'Model A' breakdown, the  $J$ - $V$  curve displays features of an exponential rise in  $J$  along with nonlinearity before the verge of breakdown and reveals a stepwise fall of  $J$  during the electrical breakdown. SEM images exhibit a single DMTNT (b) before and (c) after the breakdown.

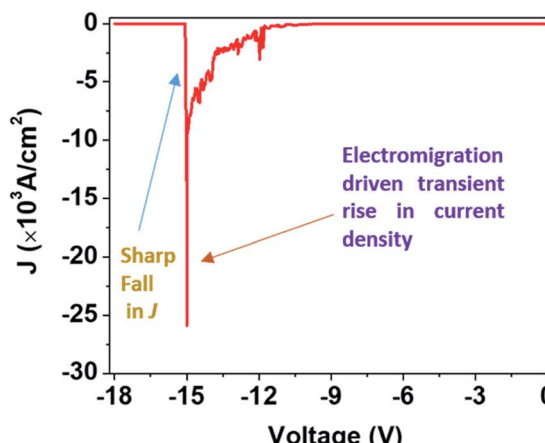
movement of charges is now governed by the creation of these cracks that are reflected in the fluctuations in the  $J$ - $V$  characteristics. It is apparent that the crack formation is dominant at the end of the nanotubes near the electrodes. This is caused by the charge injection from the contact leading to a higher probability of accumulation around this region. Such accumulation and the local heating effect at the nanotube/electrode interface<sup>53</sup> have been reported. Also, the thermal conductivity of the  $\text{TiO}_2$  NT and Au film is  $1.12 \text{ W m}^{-1} \text{ K}^{-1}$  (ref. 54) and  $160 \text{ W m}^{-1} \text{ K}^{-1}$ ,<sup>55</sup> respectively. This results in a high thermal conductance difference at the TNT-Au electrode interface (small contact area), resulting in a temperature gradient. Therefore, only the region near the end of the nanotube close to the contact reaches a very high temperature close to the melting point.

In the second type of breakdown marked 'Model B', the current density  $J$  shows a transient rise up to a maximum value ( $J_{\text{break}}$ ), followed by a sharp fall to zero (Fig. 7(a)). The morphologies of the nanotube before and after breakdown are shown in Fig. 7(b) and 7(c), respectively. A careful observation

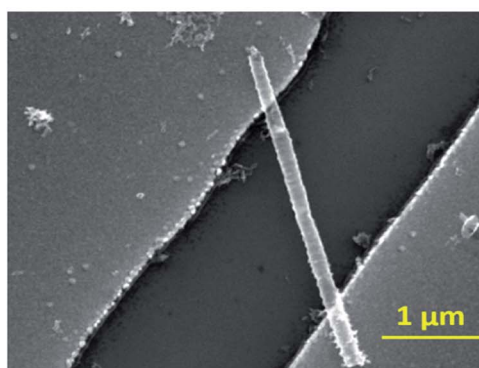
reveals that at the point of breakdown shown in Fig. 7(c), a spherical bulge is formed that indicates outward pressure on the walls of the nanotubes. We now attempt to analyze the sharp increase in the current density and consequent collapse that has not been reported so far for individual  $\text{TiO}_2$  NTs. The  $J$ - $V$  measurement (Fig. 8(a)) in the pre-breakdown region was performed by slowly increasing the bias up to the maximum point (near the breakdown voltage) and reducing it back to zero. As seen in the inset of Fig. 8(a), the  $J$ - $V$  curve is almost entirely reversible up to a bias of  $1.28 \text{ V}$ , but the noisy nature of  $J$  after this (5 to 9 V, Fig. 8(a)) may indicate reformation of the NT/Au junction region. As we increase the bias further, an abrupt increase in  $J$  occurs (9 to 10 V). However, when we decrease the bias (10 to 0 V), the  $J$ - $V$  curve almost follows the earlier pattern (0 to 10 V) but with a small upward shift (Fig. 8(a)) indicating the flow of charges along a new and less resistive path.

A further increase in the bias results in a sharp rise in  $J$  (11.3 V to 11.9 V, Fig. 8(b)) to the breakdown value ( $J_{\text{break}}$ , the value of current density at which breakdown occurs, is  $9.32 \times$

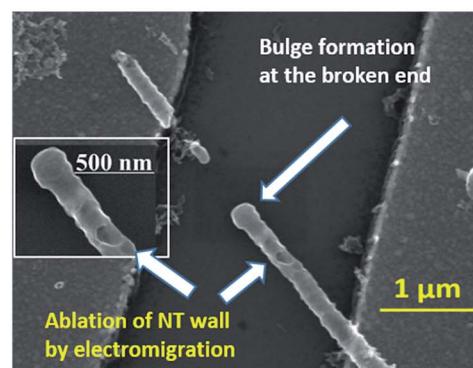




(a)



(b)



(c)

Fig. 7 (a) In the 'Model B' breakdown, the  $J$ – $V$  curve displays a sharp transient rise in  $J$  before the breakdown point and a sharp fall after the breakdown. SEM images show a single DMTNT (b) before and (c) after the breakdown. Bulge formation occurs at the broken end of the NT due to excessive heat dissipation as shown in (c); magnified image of the broken end in the inset of (c).

$10^3$  A cm $^{-2}$ ) and then it falls abruptly to zero. Such a transient increase in the current density observed in our experiments gives evidence of the occurrence of explicit, permanent changes in the nanotube at the onset of the breakdown.

A current transient observed in the 'Model B' type breakdown is attributed to a reformation of the NT–metal electrode contact. Electromigration<sup>56–58</sup> (the movement of atoms/ions under the influence of an electric field) of metal atoms under high bias is a probable cause for this type of collapse. Electric field and localized heating driven electromigration of thermally diffused metal ions from the contact and Ti ions in the nanotube leads to collapse (breakdown) at the most defective region of the wall as seen in the 'Model B' (Fig. 7(c)) breakdown. A breakdown field of  $10^4$  V cm $^{-1}$  (Fig. 7(a)) is large enough to cause electromigration in metals such as Ag, Cu, Au, In, Pb, and Mg.<sup>59</sup> Such behavior resembles the previously reported phenomenon observed in CNTs by Chiu *et al.*<sup>60</sup> As the metal ions migrate through the nanotube under high bias, they create defects and generate more heat, as a result of which the NT wall collapses with formation of a bulge as observed in Fig. 7(c) and 8(d). The asymmetric thermal gradient also plays a role in

defining the breakdown region (hottest spot) and melting the NTs at the hottest spot.<sup>61</sup>

In the case of a bundle of nanotubes, however, we observed a mixed feature of stepwise increase followed by a transient rise in  $J$  up to a maximum value. The decrease of current density also follows a mixed pattern of stepwise and sharp falls; such behavior is termed 'Model C' type breakdown (Fig. 9(a)). The FESEM images show a bundle of EGTNT before (Fig. 9(b)) and after breakdown (Fig. 9(c)). Table 3 presents typical values of breakdown voltage and current for each type of breakdown.

The chance of electrical failure becomes enhanced if there are more defects or contaminants within the NTs,<sup>62</sup> and the defect free tubes are mostly good conductors of heat. This agrees with our measurements for TNTs as we have seen that the complete or partial ablation of the NT wall occurred primarily on DMTNT during  $J$ – $V$  measurements as it has a rough wall morphology, which most probably increases the surface defects. The breakdown power in the  $\mu$ W range is sufficient to break these metal oxide nanotubes, which means they cannot sustain high power compared to extremely conducting carbon nanotubes<sup>63</sup> (mW range).



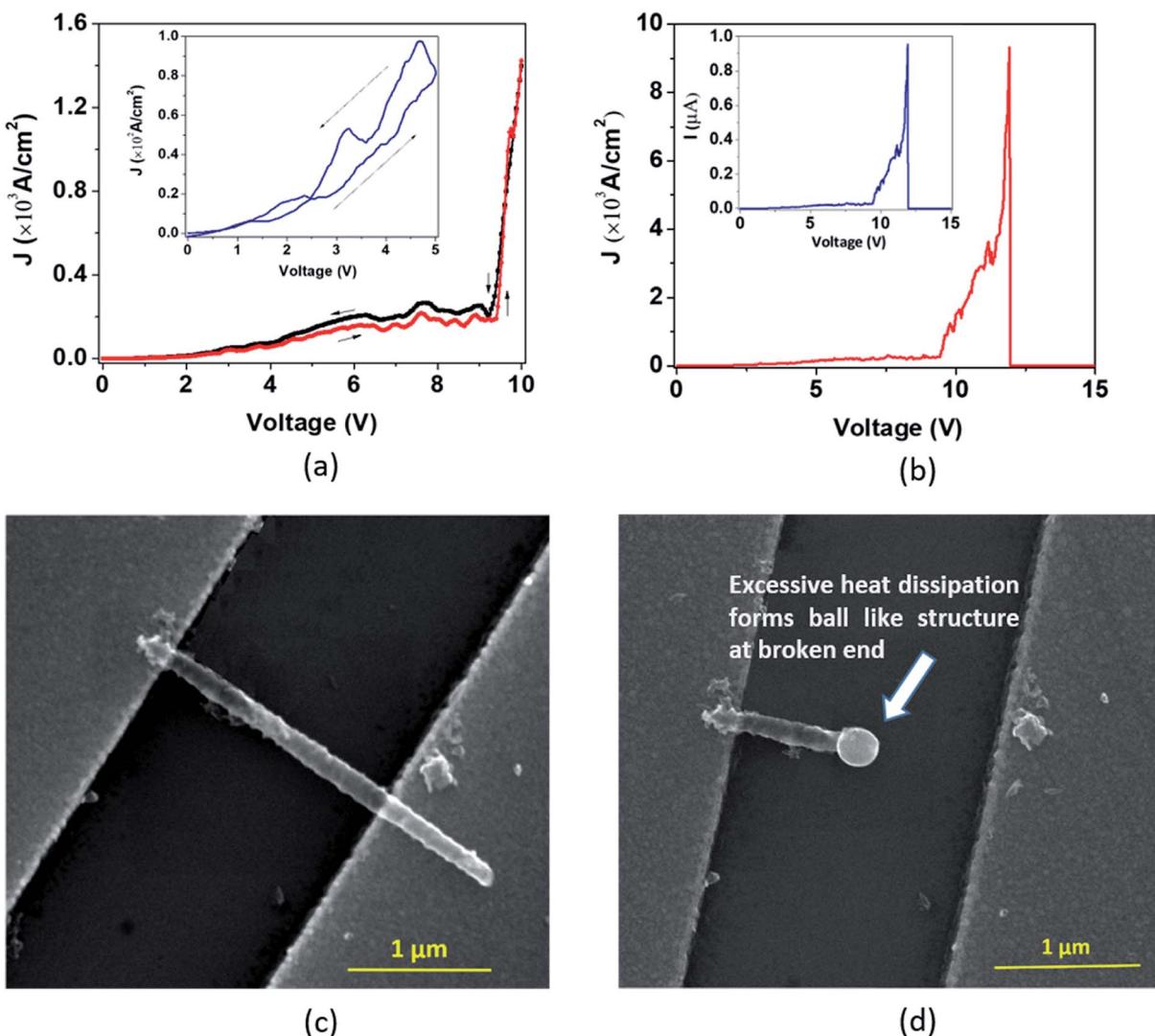


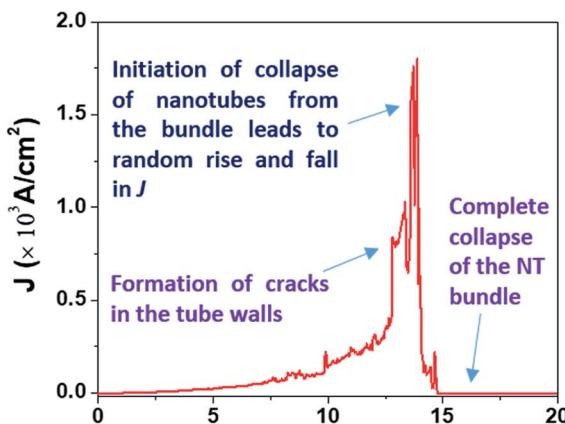
Fig. 8 (a) In 'Model B' type breakdown, gradual variation in voltage ( $0 \rightarrow 10 \text{ V} \rightarrow 0 \text{ V}$ ) before the onset of breakdown. The bias direction  $0 \rightarrow 5 \text{ V} \rightarrow 0 \text{ V}$  is shown in the inset. (b) The transient rise in  $J$  is evidence of the onset of electromigration through a single  $\text{TiO}_2$  nanotube; the  $I$ - $V$  characteristics corresponding to the  $J$ - $V$  curve are shown in the inset. The FESEM images showing an individual  $\text{TiO}_2$  nanotube (c) before and (d) after the breakdown; the breakdown point of the NT becomes distorted resulting in bulge formation as shown in (d).

As the nanotubes are suspended on two metal contact pads, the absence of a substrate beneath them constrains heat dissipation only through the surface of the NTs, the electrodes, and the neighboring environment.<sup>64</sup> As  $J$ - $V$  measurements have been performed in a vacuum atmosphere, the heat dissipation happens mostly through the NT and the electrodes. Also, it has been observed that the extremely resistive part of the NT is broken at a lower current which indicates that breakdown does not always occur at the middle part,<sup>65</sup> and also for shorter NTs, this happens away from the central part of the NT<sup>66</sup> due to the anisotropic temperature profile.

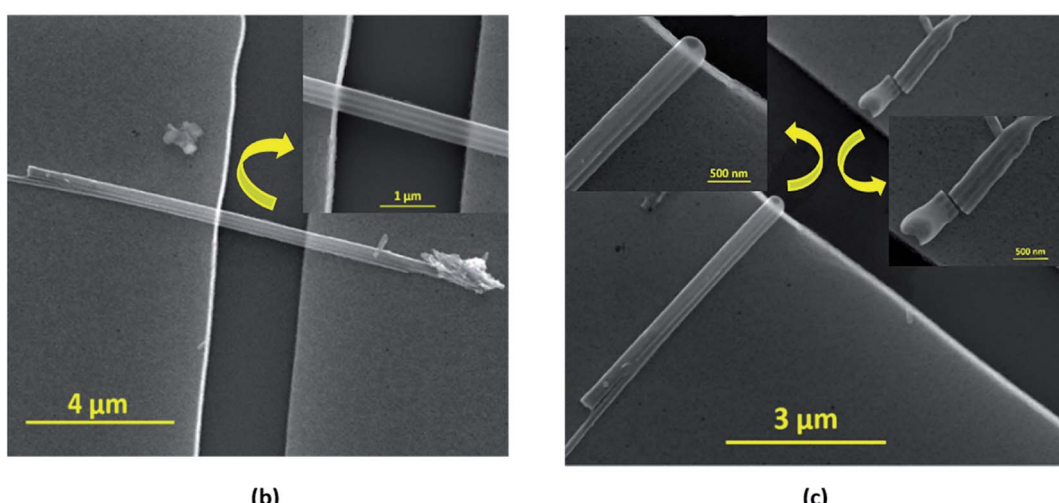
The breakdown current density  $J_{\text{break}}$  (Table 3) for a single nanotube of different morphologies may be explained using the one-dimensional thermal transport model<sup>64,65</sup> which is expressed as

$$J_{\text{break}} = \left[ \frac{\Delta T(x)\sigma\alpha\beta}{A} \right]^{1/2} \left[ 1 - \frac{1}{\cosh(\omega L/2)} \right]^{-1/2} \quad (5)$$

where  $\Delta T(x)$  is the variance between the temperature at the NT-electrode contact and the local temperature  $T(x)$  at  $x$  in the NT,  $\sigma$  is the electrical conductivity of the NT,  $\alpha$  is the contact line width,  $\beta$  is the coupling coefficient for heat transmission to the medium around the nanotube,<sup>67</sup>  $A$  is the NT cross-sectional area,  $\omega = \sqrt{\frac{\alpha\beta}{Ak}}$ ,  $k$  is the thermal conductivity of the NT, and  $L$  is the length of the NT. For our suspended NT configuration,  $J_{\text{break}} \approx 2\sqrt{\frac{2\Delta T(x)\sigma k}{L}} (\omega L \ll 1)$ ,<sup>67</sup> which shows that  $J_{\text{break}}$  is proportional to the square root of the electrical conductivity ( $\sigma$ ) and thermal conductivity of the nanotube. This explains that a lower  $J_{\text{break}}$  is sufficient to break highly resistive NTs, and this



(a)



(b)

(c)

Fig. 9 (a) In the 'Model C' breakdown, the  $J$ - $V$  curve displays mixed features of nonlinearity along with sudden big steps in  $J$  before the breakdown point which may be the characteristics for breaking of the bridge between the nanotubes in the bundle. SEM images exhibit a bundle of 3 EGTNT (b) before and (c) after the breakdown; magnified SEM images are also displayed in the insets.

Table 3 Calculated breakdown power of 'Model A', 'B' and 'C'

Type of NT breakdown	$V_{\text{break}}$ (V), $I_{\text{break}}$ (A)	Breakdown power $P_{\text{break}}$ ( $\mu\text{W}$ )
'Model A'	$10, 1.40 \times 10^{-6}$	14.6
'Model B'	$15, 2.61 \times 10^{-6}$	39.8
'Model C'	$13, 0.50 \times 10^{-6}$	6.9

is reflected in our results (Table 3) where a comparatively less conducting bundle of EGTNT breaks down at a lower  $J_{\text{break}}$  compared to individual DMTNT, supporting the one-dimensional thermal transport model.

## Conclusions

In conclusion,  $\text{TiO}_2$  nanotubes with two distinct morphologies, smooth and rough, having single and double-walled characteristics, have been successfully fabricated into individual nanotube devices. The contacts are prepared by

photolithography without using complex processes such as electron beam lithography or focused ion beam deposition. The electrical conduction process at the lower temperature regime ( $110 < T < 230$  K) and higher temperature regions ( $T > 230$  K) depends on two thermal activation processes attributed to shallow and intermediate deep donors, respectively, and the average values of the activation energies are  $E_1 \sim 122 \pm 5$  meV and  $E_2 \sim 33 \pm 1$  meV for EGTNT and  $E_1 \sim 115 \pm 4$  meV and  $E_2 \sim 28 \pm 2$  meV for DMTNT. Furthermore, the physical breakdown of the nanotubes observed at higher bias has been analyzed. The  $J$ - $V$  measurements reveal three distinct types of electrical breakdown associated with the physical collapse of the  $\text{TiO}_2$  NTs. In 'Model A' type breakdown, a stepwise rise in current density  $J$  up to the breakdown point followed by a non-uniform stepwise decrease is observed which is caused by crack formation in the NT wall. In 'Model B' type breakdown, electric field and localized heating driven electromigration of thermally diffused metal ions from the contact and Ti ions in the nanotube leads to collapse (breakdown) at the most defective region of the wall. Finally, in 'Model C' type breakdown observed in



a bundle of nanotubes, the *J-V* characteristics show mixed features of the 'Model A' and 'Model B' type breakdown. This study offers insight into the morphology dependent electrical transport in single  $\text{TiO}_2$  nanotubes and also opens up the possibility of devices based on  $\text{TiO}_2$  nanotubes. Further, the breakdown mechanisms investigated in this work help to define compliance and limitations of such nanotube devices.

## Conflicts of interest

There are no conflicts to declare.

## Acknowledgements

The authors acknowledge the Center for NEMS and Nanophotonics, IIT Madras for providing resources for fabrication and characterization and the scanning electron microscope facility (FE-SEM) partly sponsored by the DST-FIST program. SK is thankful to Deepak Bhat and Sanjoy Jena for their initial help in the fabrication and Dr Soumya Dutta and Mithun, C. A. for measurements at the cryo-probe station.

## References

- Y. Li, F. Qian, J. Xiang and C. M. Lieber, *Mater. Today*, 2006, **9**, 18–27.
- G. K. Mor, K. Shankar, M. Paulose, O. K. Varghese and C. A. Grimes, *Nano Lett.*, 2006, **6**, 215–218.
- H. S. Kim, J. W. Lee, N. Yantara, P. P. Boix, S. A. Kulkarni, S. Mhaisalkar, M. Grätzel and N. G. Park, *Nano Lett.*, 2013, **13**, 2412–2417.
- X. Duan, Y. Huang, R. Agarwal and C. M. Lieber, *Nature*, 2003, **421**, 241–245.
- W. Li, C. Liang, W. Zhou, J. Qiu, Z. Zhou, G. Sun and Q. Xin, *J. Phys. Chem. B*, 2003, **107**, 6292–6299.
- M. C. Mcalpine, H. Ahmad, D. Wang and J. R. Heath, *Nat. Mater.*, 2007, **6**, 379–384.
- J. Chen, L. Xu, W. Li and X. Gou, *Adv. Mater.*, 2005, **17**, 582–586.
- Q. Kuang, C. Lao, L. W. Zhong, Z. Xie and L. Zheng, *J. Am. Chem. Soc.*, 2007, **129**, 6070–6071.
- M. D. Kelzenberg, D. B. Turner-Evans, B. M. Kayes, M. A. Filier, M. C. Putnam, N. S. Lewis and H. A. Atwater, *Nano Lett.*, 2008, **8**, 710–714.
- J. Bao, M. A. Zimmler, F. Capasso, X. Wang and Z. F. Ren, *Nano Lett.*, 2006, **6**, 1719–1722.
- S. J. Tans, A. R. M. Verschueren and C. Dekker, *Nature*, 1998, **393**, 49–52.
- A. L. Linsebigler, G. Lu and J. T. Yates, *Chem. Rev.*, 1995, **95**, 735–758.
- D. Deng, M. G. Kim, J. Y. Lee and J. Cho, *Energy Environ. Sci.*, 2009, **2**, 818–837.
- M. H. Seo, M. Yuasa, T. Kida, J. S. Huh, K. Shimano and N. Yamazoe, *Sens. Actuators, B*, 2009, **137**, 513–520.
- S. Rani, S. C. Roy, M. C. Bhatnagar and D. Kanjilal, in *Proceedings of IEEE Sensors*, 2008.
- S. U. M. Khan, M. Al-Shahry and W. B. Ingler, *Science*, 2002, **297**, 2243–2245.
- G. K. Mor, K. Shankar, M. Paulose, O. K. Varghese and C. A. Grimes, *Nano Lett.*, 2005, **5**, 191–195.
- A. Fujishima and K. Honda, *Nature*, 1972, **238**, 37–38.
- P. Chen, J. Brillet, H. Bala, P. Wang, S. M. Zakeeruddin and M. Grätzel, *J. Mater. Chem.*, 2009, **19**, 5325–5328.
- B. Oregan and M. Gratzel, *Nature*, 1991, **353**, 737–740.
- O. K. Varghese, M. Paulose and C. A. Grimes, *Nat. Nanotechnol.*, 2009, **4**, 592–597.
- S. Farsinezhad, A. Mohammadpour, A. N. Dalrymple, J. Geisinger, P. Kar, M. J. Brett and K. Shankar, *J. Nanosci. Nanotechnol.*, 2013, **13**, 2885–2891.
- S. Rani, S. C. Roy, M. Paulose, O. K. Varghese, G. K. Mor, S. Kim, S. Yoriya, T. J. Latempa and C. A. Grimes, *Phys. Chem. Chem. Phys.*, 2010, **12**, 2780–2800.
- K. Lee, A. Mazare and P. Schmuki, *Chem. Rev.*, 2014, **114**, 9385–9454.
- H. Tsuchiya and P. Schmuki, *Nanoscale*, 2020, **12**, 8119–8132.
- C. Fàbrega, F. Hernández-Ramírez, J. Daniel Prades, R. Jiménez-Díaz, T. Andreu and J. Ramon Morante, *Nanotechnology*, 2010, **21**, 445703.
- M. Stiller, J. Barzola-Quiquia, I. Lorite, P. Esquinazi, R. Kirchgeorg, S. P. Albu and P. Schmuki, *Appl. Phys. Lett.*, 2013, **103**, 1–5.
- M. Hattori, K. Noda, T. Nishi, K. Kobayashi, H. Yamada and K. Matsushige, *Appl. Phys. Lett.*, 2013, **102**, 1–5.
- M. Lee, D. Cha, J. Huang, M.-W. Ha and J. Kim, *Jpn. J. Appl. Phys.*, 2016, **55**, 06GG11.
- H. Brahmi, R. Neupane, L. Xie, S. Singh, M. Yarali, G. Katwal, S. Chen, M. Paulose, O. K. Varghese and A. Mavrokefalos, *Nanoscale*, 2018, **10**, 3863–3870.
- S. Yoriya, M. Paulose, O. K. Varghese, G. K. Mor and C. A. Grimes, *J. Phys. Chem. C*, 2007, **111**, 13770–13776.
- S. P. Albu and P. Schmuki, *Phys. Status Solidi RRL*, 2010, **4**, 215–217.
- D. Cha, M. Lee, H. Shin, M. J. Kim and J. Kim, *Microsc. Microanal.*, 2009, **15**, 1180–1181.
- M. Enachi, O. Lupan, T. Braniste, A. Sarua, L. Chow, Y. K. Mishra, D. Gedamu, R. Adelung and I. Tignyanu, *Phys. Status Solidi RRL*, 2015, **9**, 171–174.
- D. Wisniewski, K. Byrne, C. F. De Souza, C. Fernandes and H. E. Ruda, *Nanotechnology*, 2019, **30**, 054007.
- C. Opoku, A. S. Dahiya, G. Poulin-Vittrant, N. Camara and D. Alquier, *Phys. Status Solidi A*, 2016, **213**, 2438–2445.
- P. P. Vijayan, M. Thomas and K. C. George, *J. Appl. Phys.*, 2012, **112**, 104308.
- C. Jia, F. Yang, L. Zhao, G. Cheng and G. Yang, *Nanoscale Res. Lett.*, 2019, **14**, 10.
- L. Hu, L. Wu, M. Liao, X. Hu and X. Fang, *Adv. Funct. Mater.*, 2012, **22**, 998–1004.
- L. Q. Mai, C. S. Lao, B. Hu, J. Zhou, Y. Y. Qi, W. Chen, E. D. Gu and Z. L. Wang, *J. Phys. Chem. B*, 2006, **110**, 18138–18141.
- J. R. Yeargan and H. L. Taylor, *J. Appl. Phys.*, 1968, **39**, 5600–5604.



42 W. Yang, J. Marino, A. Monson and C. A. Wolden, *Semicond. Sci. Technol.*, 2006, **21**, 1573–1579.

43 I. Ali, M. Suhail, Z. A. Alothan and A. Alwarthan, *RSC Adv.*, 2018, **8**, 30125–30147.

44 J. Kuchařík, H. Sopha, M. Krbal, I. Rychetský, P. Kužel, J. M. Macák and H. Němec, *J. Phys. D: Appl. Phys.*, 2018, **51**, 014004.

45 R. Mohammadpour, *J. Phys. D: Appl. Phys.*, 2017, **50**, 505106.

46 R. S. Chen, C. A. Chen, W. C. Wang, H. Y. Tsai and Y. S. Huang, *Appl. Phys. Lett.*, 2011, **99**, 2011–2014.

47 J. M. Baik, M. H. Kim, C. Larson, X. Chen, S. Guo, A. M. Wodtke and M. Moskovits, *Appl. Phys. Lett.*, 2008, **92**, 90–93.

48 A. Rothschild, Y. Komem, A. Levakov, N. Ashkenasy and Y. Shapira, *Appl. Phys. Lett.*, 2003, **82**, 574–576.

49 R. S. Chen, C. A. Chen, W. C. Wang, H. Y. Tsai and Y. S. Huang, *Appl. Phys. Lett.*, 2011, **99**, 222107.

50 N. Liu, H. Mirabolghasemi, K. Lee, S. P. Albu, A. Tighineanu, M. Altomare and P. Schmuki, *Faraday Discuss.*, 2013, **164**, 107–116.

51 H. Mirabolghasemi, N. Liu, K. Lee and P. Schmuki, *Chem. Commun.*, 2013, **49**, 2067–2069.

52 X. Tian, G. L. Brennecke and X. Tan, *ACS Nano*, 2020, **14**, 8328–8334.

53 M. M. Yazdanpanah, S. Chakraborty, S. A. Harfenist, R. W. Cohn and B. W. Alpnenaar, *Appl. Phys. Lett.*, 2004, **85**, 3564–3566.

54 L. Guo, J. Wang, Z. Lin, S. Gacek and X. Wang, *J. Appl. Phys.*, 2009, **106**, 123526.

55 Q. G. Zhang, B. Y. Cao, X. Zhang, M. Fujii and K. Takahashi, *Phys. Rev. B: Condens. Matter Mater. Phys.*, 2006, **74**, 1–5.

56 W. Y. Jang, N. N. Kulkarni, C. K. Shih and Z. Yao, *Appl. Phys. Lett.*, 2004, **84**, 1177–1179.

57 A. Fujii, M. Tsutsui, S. Kurokawa and A. Sakai, *Phys. Rev. B: Condens. Matter Mater. Phys.*, 2005, **72**, 1–6.

58 H. Park, A. K. L. Lim, A. P. Alivisatos, J. Park and P. L. McEuen, *Appl. Phys. Lett.*, 1999, **75**, 301–303.

59 H. M. Breitling, *J. Phys. Chem. Solids*, 1972, **33**, 845–852.

60 H. Y. Chiu, V. V. Deshpande, H. W. C. Postma, C. N. Lau, C. Mikó, L. Forró and M. Bockrath, *Phys. Rev. Lett.*, 2005, **95**, 1–4.

61 C. Kim, D. Kang, T. Y. Lee, K. H. P. Kim, Y. S. Kang, J. Lee, S. W. Nam, K. B. Kim and Y. Khang, *Appl. Phys. Lett.*, 2009, **94**, 92–95.

62 P. Poncharal, C. Berger, Y. Yi, Z. L. Wang and W. A. De Heer, *J. Phys. Chem. B*, 2002, **106**, 12104–12118.

63 M. Tsutsui, Y. K. Taninouchi, S. Kurokawa and A. Sakai, *J. Appl. Phys.*, 2006, **100**, 094302.

64 M. A. Kuroda, A. Cangellaris and J. P. Leburton, *Phys. Rev. Lett.*, 2005, **95**, 1–4.

65 G. K. Goswami and K. K. Nanda, *AIP Adv.*, 2012, **2**, 022129.

66 A. Liao, R. Alizadegan, Z. Y. Ong, S. Dutta, F. Xiong, K. J. Hsia and E. Pop, *Phys. Rev. B: Condens. Matter Mater. Phys.*, 2010, **82**, 1–9.

67 H. Kitsuki, T. Yamada, D. Fabris, J. R. Jameson, P. Wilhite, M. Suzuki and C. Y. Yang, *Appl. Phys. Lett.*, 2008, **92**, 2006–2009.

